Tectonophysics 823 (2022) 229193

Contents lists available at ScienceDirect

Tectonophysics

journal homepage: www.elsevier.com/locate/tecto

Dense seismological array and profile across the Longmenshan and the deep extension of the Pengguan complex

Hui Qian [a,*], Changqing Yu [a], James Mechie [b], Xiangzhi Zeng [a]

[a] Key Laboratory of Deep-Earth Dynamics of Ministry of Natural Resources, Institute of Geology, Chinese Academy of Geological Sciences, China
[b] Deutsches GeoForschungsZentrum – GFZ, Section "Geophysical Imaging", Telegrafenberg, 14473 Potsdam, Germany

ARTICLE INFO

Keywords:
Receiver functions
P-wave tomography
Tibet plateau
Longmenshan fault zone
Asia

ABSTRACT

A dense seismological array and profile reveal the deep structure across the Longmenshan from the Songpan-Ganzi terrane of the Tibetan plateau to the Sichuan basin. Receiver function and tomographic images reveal that the Pengguan Complex which cores the Longmenshan in the region where the Ms. 8 Wenchuan earthquake of 2008 occurred, is marked by high velocities in the upper 15 km of the crust. At about 15 km depth both P- and S-wave velocities decrease at a flat-lying boundary around which the aftershock hypocentres of the Wenchuan earthquake are concentrated. Thus, this boundary may be a faulted interface or detachment, marking the base of the Pengguan Complex. Moho depths change significantly in going from the Tibetan plateau to the Sichuan basin. At the location of the dense profile a Moho step occurs, located about 50 km NW of the surface trace of the Yingxiu-Beichuan fault (YBF). The boundary at about 15 km depth below the Pengguan Complex seems to deepen at around the Wenchuan-Maoxian fault (WMF) by about 3 km and merge to the NW with another interface at about 18 km depth. This interface, NW of the WMF, which correlates with the top of a zone of high conductivity is interpreted to represent the top of the Tibetan mid-crustal low velocity, high conductivity zone. The tomographic image indicates that the boundary between the low velocities of the Songpan-Ganzi terrane and the high velocities of the Sichuan basin in the middle and lower crust occurs NW of the surface trace of the YBF. Thus, it is proposed that a zone extending from the WMF at about 15 km depth to the Moho step about 25 km further NW marks the boundary between the Tibetan plateau and the Sichuan basin in the middle and lower crust.

1. Introduction

The Longmenshan fault zone forms the eastern boundary of the Tibetan plateau, to the southeast of which the Sichuan basin occurs. The Longmenshan is cut by a series of faults striking SW-NE, which form the Longmenshan fault zone. They are the Wenchuan-Maoxian Fault (WMF), Yingxiu-Beichuan Fault (YBF), Anxian-Guanxian Fault (AGF) and Guankou Fault from west to east respectively. GPS observations show that the convergence rate in the Longmenshan area is relatively small at about 4 ± 2 mm/a (Zhang et al., 2004). However, the surface deformation caused by the Wenchuan earthquake is enormous. The duration of the rupture lasted 90 s, maximum slip reached 7 m, the rupture length of the Longmenshan Fault was over 300 km (Li et al., 2013) and it killed 69,000 people. It is noted that less than 100 km away from the Longmenshan is the city of Chengdu with a population of around 14,000,000 inhabitants. Therefore, further study of the Longmenshan seismogenic fault, especially the crustal and upper mantle structure in the vicinity and the deep driving mechanism of the fault, is of great significance for earthquake prevention and disaster reduction.

The Pengguan Complex and Baoxing Complex bounded by the Longmenshan fault zone comprise Precambrian folded crystalline basement (Cook et al., 2013). In the remaining areas of the Longmenshan, mainly Precambrian and Paleozoic rocks are exposed. To the west of the Longmenshan, an important component of the Tibetan plateau, the Songpan-Ganzi terrane occurs, composed of Triassic flysch sediments, whose thickness generally exceeds 10 km and locally reaches 15 km (Weislogel, 2008). The Sichuan basin to the east of the Longmenshan comprises up to 12–13 km of Late Proterozoic to Quaternary sediments in the study region (Wang et al., 2016). As a block which formed earlier than the Longmenshan fault zone, the Pengguan Complex is controlled by the YBF along its southeast boundary and the WMF along its northwest boundary. Ma et al. (1996) postulated that the

* Corresponding author.
E-mail address: huiqian@aliyun.com (H. Qian).

https://doi.org/10.1016/j.tecto.2021.229193
Received 2 February 2021; Received in revised form 9 July 2021; Accepted 23 December 2021
Available online 29 December 2021

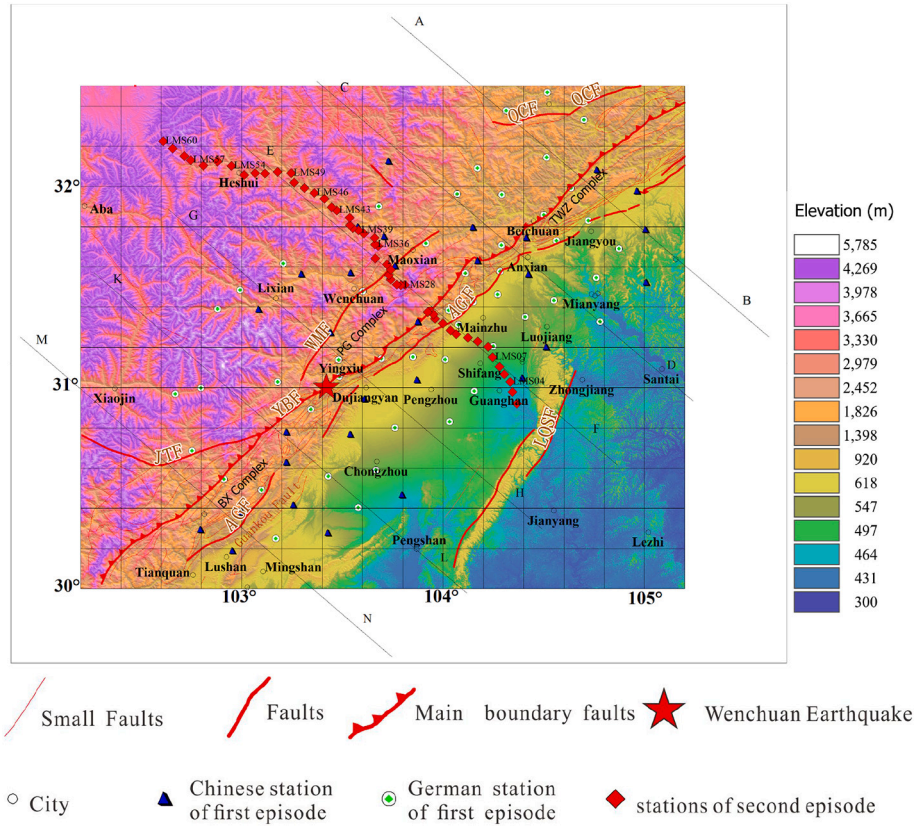

Fig. 1. Location map of stations and main faults.
WMF Wenchuan-Maoxian Fault; YBF Yingxiu-Beichuan Fault; AGF Anxian-Gaunxian Fault; JTF Jingtang Arc Fault; QCF Qingchuan Fault; LQSF Longquanshan Fault; TWZ Complex -Tangwangzhai Complex; PG Complex -Pengguan Complex; BX Complex -Baoxing Complex.

Pengguan Complex is an old klippe with strong deformation. Liu and Lin (2008) proposed that it developed as an intrusion more or less in the same position as it is found today and that it was then brought to the surface by thrust faults. Burchfiel et al. (1995) also considered that the shortening and lateral movement of the upper crust in the Longmenshan during the Cenozoic was limited. The YBF was the main fault activated by the Wenchuan earthquake, while the WMF only experienced small deformation during the earthquake, which demonstrates that the two faults on either side of the Pengguan Complex can react differently during any single earthquake.

Before the Wenchuan earthquake, geophysical surveys in the Longmenshan area were few (Wang et al., 2007). In contrast, after the Wenchuan earthquake a lot of geophysical and geological surveys have been conducted (Zhang et al., 2009, 2010; Robert et al., 2010; Li et al., 2010, 2013, 2014a, 2014b, 2016; Cook et al., 2013; Guo et al., 2013; Liu et al., 2014; Wang et al., 2015a; Wu et al., 2014; Xu et al., 2016). However, there is still no unified understanding about the deep extension of the Longmenshan fault zone and hence the base of the Pengguan Complex. Within the framework of the Wenchuan earthquake Fault Scientific Drilling project, the borehole WFSD-1 cut the YBF at a depth of 600–760 m and determined that the fault has a dip angle of about 70° down to that depth (Li et al., 2013). Above the fault the borehole passed through the Pengguan Complex and below the fault Triassic rocks. The borehole WFSD-2, about 300 m NW of WFSD-1, cut the YBF at about 1700 m depth (Lu et al., 2014), indicating that the dip angle of about 70° continues down to this depth. Integrating geological investigations, relocated aftershocks of the Wenchuan earthquake and seismic reflection profiles, Jia et al. (2010) and Li et al. (2010) provided evidence that the segment of the YBF southwest of Anxian (Fig. 1) dips at 30–45° to the NW and soles into a detachment at 15–17 km depth. However, as the reflection profiles only extend to a maximum of 15 km depth and a few kilometres distance into the Pengguan complex, the continuation of the detachment to the NW is still largely unknown. Tomographic studies have shown that high velocities are associated with the Pengguan Complex in the upper crust (Wang et al., 2015b; Feng et al., 2021).

With respect to how the boundary between the Sichuan basin and the Tibetan plateau extends through the middle and lower crust, Guo et al. (2013), from a near-vertical incidence reflection profile that crossed the Longmenshan fault zone at about 31.6°N, showed the Longmenshan fault cutting through the crust at a high angle to connect the point where the WMF and YBF join at depth to a small step in the Moho about 30 km to the NW. From magnetotelluric studies across the Longmenshan fault zone in the region, Zhao et al. (2012) found a layer with high conductivity beneath the eastern Tibetan plateau, that terminates about 25 km NW of the WMF and whose top occurs at about 20 km depth. Qian et al. (2018), based on receiver function analysis, found a negative converter indicating a decrease of velocity downwards at about the same depth to the NW of the Longmenshan beneath the Tibetan plateau. From local earthquake tomography, Wang et al. (2015b) found lower velocities beneath the Tibetan plateau to the NW of the Longmenshan than beneath the Sichuan basin in the middle and lower crust.

At Moho level, the Moho deepens and the crust thickens when going from the Sichuan basin to the Tibetan plateau. Southeast of 31.5°N along the YBF, studies using controlled sources (e.g. Jia et al., 2014; Wang et al., 2007, 2013, 2015a) show a smoother deepening of the Moho than studies using passive sources (e.g. Liu et al., 2014; Qian et al., 2018; Robert et al., 2010; Zhang et al., 2009, 2010). Northwest of 31.5°N, studies using controlled sources (Guo et al., 2013; Xu et al., 2016) and a study using passive sources (Qian et al., 2018) show a relatively smooth deepening of the Moho. From the studies of Liu et al. (2014), Qian et al. (2018), Robert et al. (2010) and Zhang et al. (2009, 2010), results for cross-sections across the YBF at about 31°N all show an abrupt

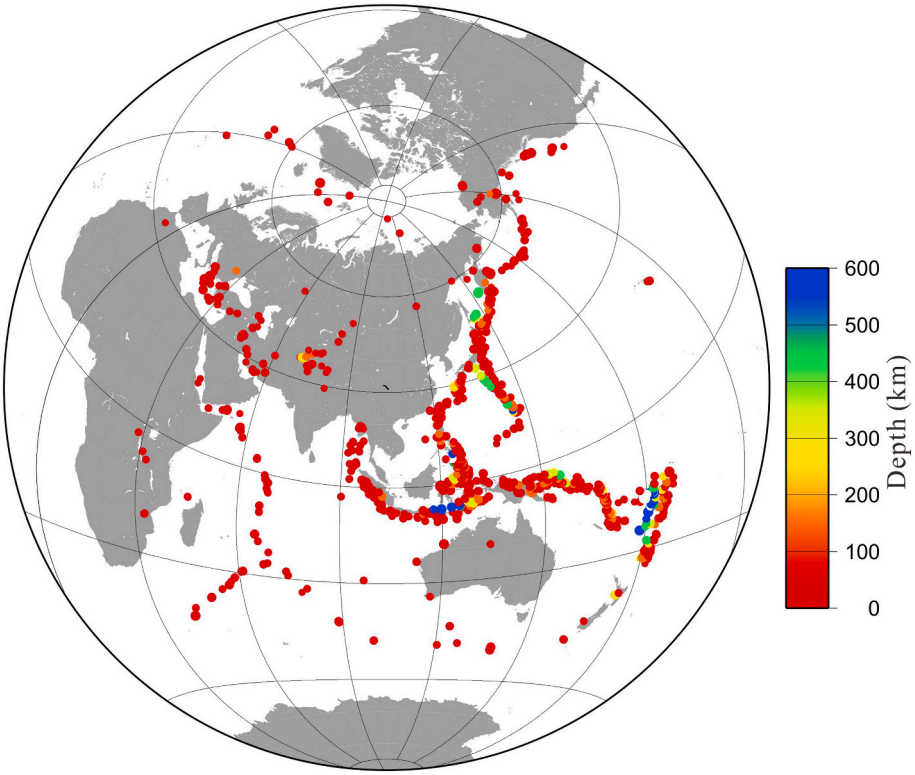

Fig. 2. Map showing the distribution of earthquakes (coloured dots according to depth) used for receiver function analysis during the deployment period from 2018 to 2020.

deepening of or a step in the Moho of 15–30 km. Further, the abrupt deepening or step always occurs NW of the Longmenshan fault zone and not SE of it.

2. Data

Firstly, between June 2012 and October 2013, the Chinese Academy of Geological Sciences (CAGS) and Deutsches GeoForschungsZentrum (GFZ) deployed a dense array of 80 stations in the Longmenshan area. During the deployment, the Lushan earthquake occurred in April 2013 at the southwest end of the array. Relocation of this earthquake demonstrated that it is not an aftershock of the Wenchuan earthquake (Qian et al., 2016). Secondly, between May 2018 and January 2020, a dense profile of 49 stations was deployed across the Longmenshan fault zone and Pengguan Complex to record passive sources (Fig. 1). In detail the profile extended from Guanghan in the southeast via Shifang to Mianzhu, then crossed the AGF and YBF into the Pengguan Complex, and then continued from Maoxian to the northwest of Heshui. This profile almost coincided with section *E*-F of the first deployment (Fig. 1). In this study the results of a *P* receiver function analysis and a tomographic analysis for P-wave velocities using both local and teleseismic events are presented. Using these methods it is not possible to image the steeply dipping faults of the Longmenshan fault zone. Rather, the purpose of this study is to investigate the depth extent of the Pengguan Complex, possible differences in the velocity structure in the middle and lower crust between the Songpan-Ganzi terrane of the Tibetan plateau and the Sichuan basin and further investigate the Moho structure.

At the same time, the CAGS carried out a deep seismic reflection profile in the Lushan area, which obtained the deep structure of the hypocentral region of the Lushan earthquake and the basal structure of the fold belt exposed at the surface (Feng et al., 2016). As for the Wenchuan earthquake, there has been no such detailed work to probe its seismogenic fault. As the core of the Longmenshan in the Wenchuan area is the Pengguan Complex at an altitude of 4000–5000 m, explosion seismic operations are almost impossible. However, even although deep seismic reflection profiles in the Wenchuan area are absent in the Pengguan Complex, through increasing shot-point density and the offset of the observation systems in the neighbourhood, deep information was successfully retrieved. Interpretation of the existing seismic profiles considered that the Pengguan Complex is deep basement brought up by compressional movements and cut by a basal fault (Yu et al., 2021). If, in fact, the Pengguan Complex is terminated by a more or less horizontal, basal fault (Li et al., 2010; Yu et al., 2021) and the material below the fault has a significantly different velocity with respect to that of the Pengguan Complex, then it is possible that this velocity contrast can be detected by the methods used in this study. Thus, this study could provide evidence, although somewhat indirect, for a more or less flat-lying detachment at the base of the Pengguan Complex.

3. Receiver function analysis

In order to obtain receiver functions for the data recorded along the profile during the second deployment period between 2018 and 2020, the data were processed in the same manner as those from the first deployment period between 2012 and 2013 (Qian et al., 2018). The data obtained between 2018 and 2020 were recorded continuously at 100 samples per second. From global earthquake catalogues, 1209 teleseismic events with epicentral distances ranging from 30° to 90° and magnitudes greater than or equal to 5.0 were selected (Fig. 2). Most of these events occur to the east of the array but a respectable number also occur to the west (Fig. 2). The data for these events were extracted from the continuous data recordings and were processed for the *P* receiver function analysis. In doing so, the Computer Programs in Seismology package by Herrmann (2013) was partly utilized. Processing steps included band-pass filtering from 1.25–20 s and rotation from the coordinate system (vertical, NS horizontal, EW horizontal) in which the data were recorded to a ray-based (*P*, *SV*, *SH* or L, Q, T) coordinate system (Qian et al., 2018 and references therein). The rotation angles

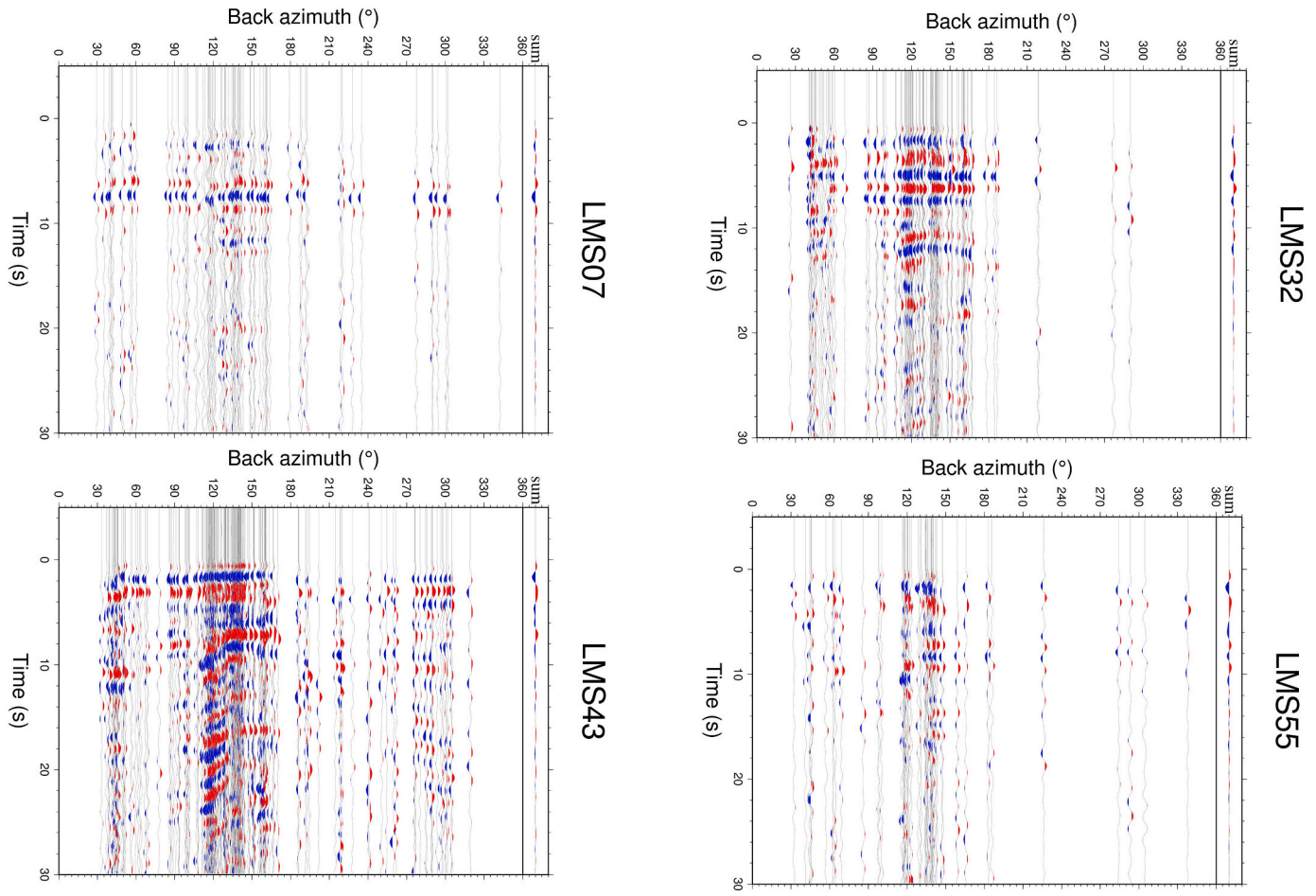

Fig. 3. Examples of *P* receiver functions from four stations, LMS07, LMS32, LMS43 and LMS55 along the profile deployed between 2018 and 2020. The traces have been band-pass filtered from 1.25 to 20 s and are plotted with moveout correction and according to the back azimuth. The summed trace is shown to the right in each case.

were obtained from the back azimuth angle for the horizontal angle and the covariance matrix of the vertical and radial components of the *P*-wave group for the vertical angle (Kind et al., 1995). In doing so, the best angle of incidence minimizes the *P*-wave energy on the *SV* component (Kumar et al., 2006). In the best case, it will eliminate the *P*-wave energy on the *SV* component. The next step was an iterative time domain deconvolution of the *SV* component by the *P* component, in which only traces with a signal-to-noise ratio greater than 1.5 were accepted and deconvolved. Noise was defined as the 70 s before the onset time of the first *P*-wave while signal was defined as the first 160 s following the onset time of the first *P*-wave. Following the deconvolution a further automatic selection for good quality traces was carried out, involving two steps. Firstly, receiver functions with anomalously large peaks in the *P*-wave coda were discarded. Secondly, a comparison with the final stacked receiver function for the respective station was carried out and the trace was only accepted if the correlation coefficient was greater than 0.25. Finally, each individual receiver function was visually inspected and traces with no *P* to *S* (*Ps*) conversion at the Moho or with strong low-frequency oscillations were omitted, which resulted in 9025 suitable *P* receiver functions. For summation of many traces in the time domain, a distance move-out correction with respect to a reference epicentral distance of 67° (reference slowness of 6.4 s per degree) was performed (Yuan et al., 1997), using a simplified version of the IASP91 velocity model (Kennett and Engdahl, 1991), with the Moho at 65 km depth (Qian et al., 2018). For stations in the Sichuan basin where the Moho occurs at about 47 km depth, Qian et al. (2018) have shown that it makes little difference whether the distance move-out correction is applied with the Moho at 47 km depth as opposed to 65 km depth.

Receiver functions are shown for four stations along the 2018–2020 profile (Fig. 3). The first station, LMS07, is located to the SE of the Longmenshan fault zone in the Sichuan basin where, according to Wang et al. (2016), the thickness of the Mesozoic sediments with P-wave velocities between 4.6 and 5.6 km/s is about 9.4 km. The second station, LMS32, is located at the WMF on the back (NW) side of the Pengguan complex. The other two stations, LMS43 and LMS55, are both situated NW of the Longmenshan, in the Songpan-Ganzi terrane of the Tibetan plateau. The station LMS07 is characterized by four positive and three negative pulses up to 9 s delay time in the summed trace. The positive pulse at about 1.5 s delay time may represent the *Ps* conversion from the base of the Mesozoic sediments where, according to Wang et al. (2016), the S-wave velocity increases abruptly by about 0.35 km/s. Using the velocity-depth profile of Wang et al. (2016) in the vicinity of station LMS07 the conversion time of 1.5 s corresponds to a thickness for the Mesozoic sediments of about 9.2 km, which is within 0.2 km of the value determined by Wang et al. (2016). The positive pulse at about 6.2 s delay time can be observed on many of the individual traces and is the most prominent positive pulse in the summed trace. It probably represents the *Ps* conversion from the Moho which would then imply a crustal thickness of about 49–50 km. This agrees with the crustal thickness obtained from previous receiver function studies in this part of the Sichuan basin (e.g. Robert et al., 2010; Zhang et al., 2010; Liu et al., 2014; Qian et al., 2018). The small negative pulse at about 5 s delay time was also recognized in the 2012–2013 data (Qian et al., 2018). Although the other pulses between about 2 and 4 s and between 7 and 9 s delay time

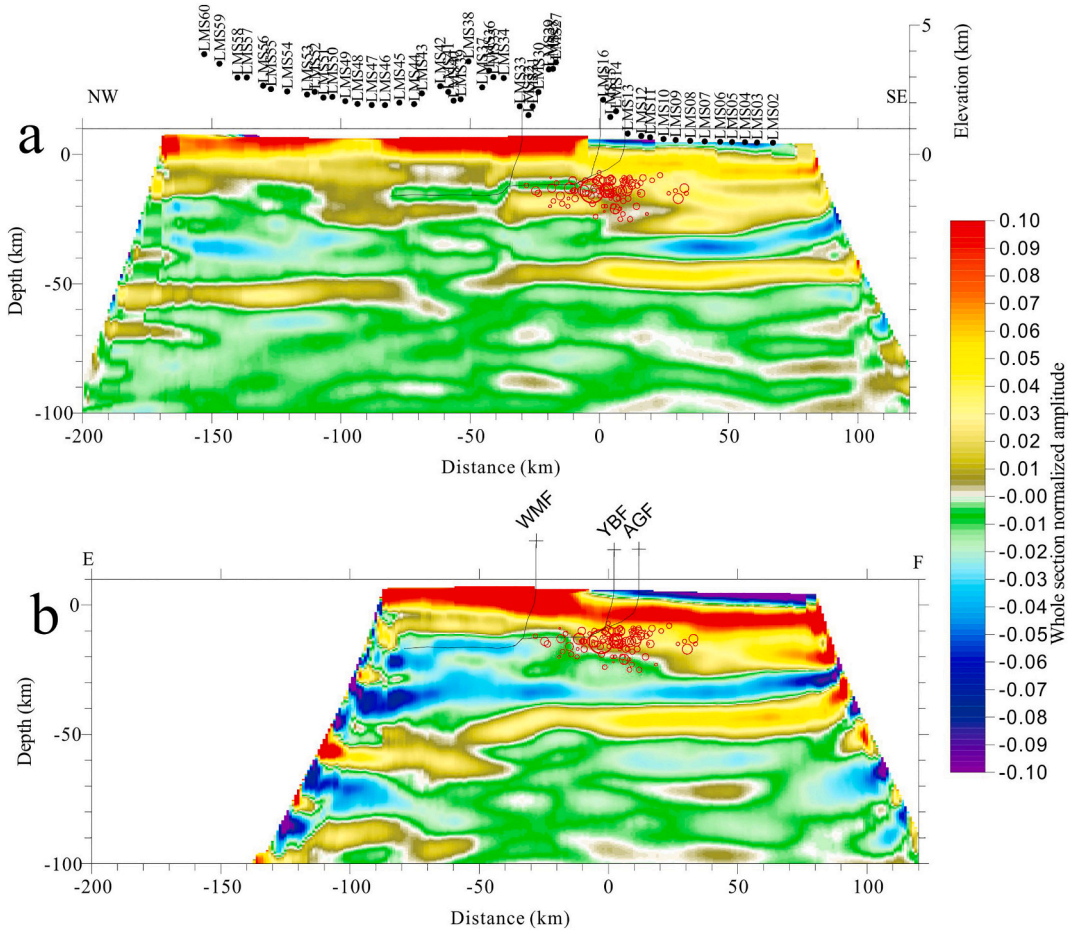

Fig. 4. Comparison of receiver function migration between the two periods of collected data.
a) Receiver function result of second period from 2018 to 2020. The elevation of the station is marked by the dot below the station name. b) Receiver function result of first period from 2012 to 2013.
Circles represent the aftershocks of the Wenchuan earthquake whose magnitudes are larger than 4, with circle size scaled according to magnitude. Thin black lines represent faults whose abbreviations are as in Fig. 1.

could be recognized on some of the individual traces in the 2012–2013 data, they did not show up as prominently in the summed traces as they do in the summed trace for station LMS07 (Fig. 3). The most prominent positive pulse in the summed trace for station LMS32 occurs at about 6.3 s delay time. It probably represents the *Ps* conversion from the Moho which would then imply a crustal thickness of about 50 km. The positive pulse at about 1 s delay time may represent the *Ps* conversion from the base of the Paleozoic and Precambrian sediments which are exposed at this location just SE of the WMF. Between 1.5 and 6 s delay time, a negative pulse at about 1.75 s delay time, corresponding to a depth of about 14 km, is followed by a broad positive pulse and another negative pulse. The receiver function phases for the two stations, LMS43 and LMS55, situated in the Songpan-Ganzi terrane show less coherency than those for the stations LMS07 and LMS32 (Fig. 3). The summed traces for stations LMS43 and LMS55 both show a positive pulse at about 0.7 s delay time, which is probably the *Ps* conversion marking the base of the Songpan-Ganzi flysch deposits. The summed trace for station LMS43 shows a positive pulse at about 7 s delay time. This pulse is mainly due to the dominance of traces from back azimuths between 110 and 160° and is probably due to the *Ps* conversion from the Moho. It implies a crustal thickness of about 56 km. Between 4 and 6.5 s delay time, two small negative pulses are observed, especially in the summed trace and between 1.5 and 4 s delay time a negative pulse at about 1.75 s delay time followed by a rather broad positive pulse can be recognized, again especially in the summed trace. Station LMS55 has fewer traces than the other three stations. The summed trace for this station again shows a positive pulse at about 7 s delay time. This pulse is mainly due to the dominance of traces from back azimuths between 110 and 190°. If this pulse represents the *Ps* conversion from the Moho, it implies a crustal thickness of about 56 km, as for station LMS43. Between 5 and 6.5 s delay time, a broad negative pulse is observed, especially in the summed trace. Between 1.5 and 5 s delay time, a negative pulse at about 1.75 s delay time followed by a broad positive pulse can be recognized, especially in the summed trace, similar to station LMS43.

As for the 2012–2013 data, a time to depth migration of the *P* receiver functions obtained from the 2018–2020 data has been carried out (Fig. 4a). For this purpose a backward propagation along the ray (Yuan, 2000) modified to account for the station elevation and the near-station ray-path differences was utilized. The backward propagation along the ray, which is similar to the common conversion point method of Dueker and Sheehan (1997, 1998), was carried out using ray-tracing through the same simplified version of the IASP91 velocity model (Kennett and Engdahl, 1991) as was used above, with P and S velocities at the surface of 5.2 and 3.2 km/s respectively and with the Moho at 65 km depth. Whereas this is an appropriate depth for the stations on the Tibetan plateau, it is considerably larger than the Moho depth for stations in the Sichuan basin. However, Qian et al. (2018) showed that a migration with the Moho at 47 km depth made little difference and that the maximum difference in Moho depths does not exceed 3.5 km. Firstly, migration was carried out along the event-receiver back azimuth and the amplitudes for specific depths were entered into boxes along the 2-D profile. These boxes were 12 km long in the profile direction, 250 km

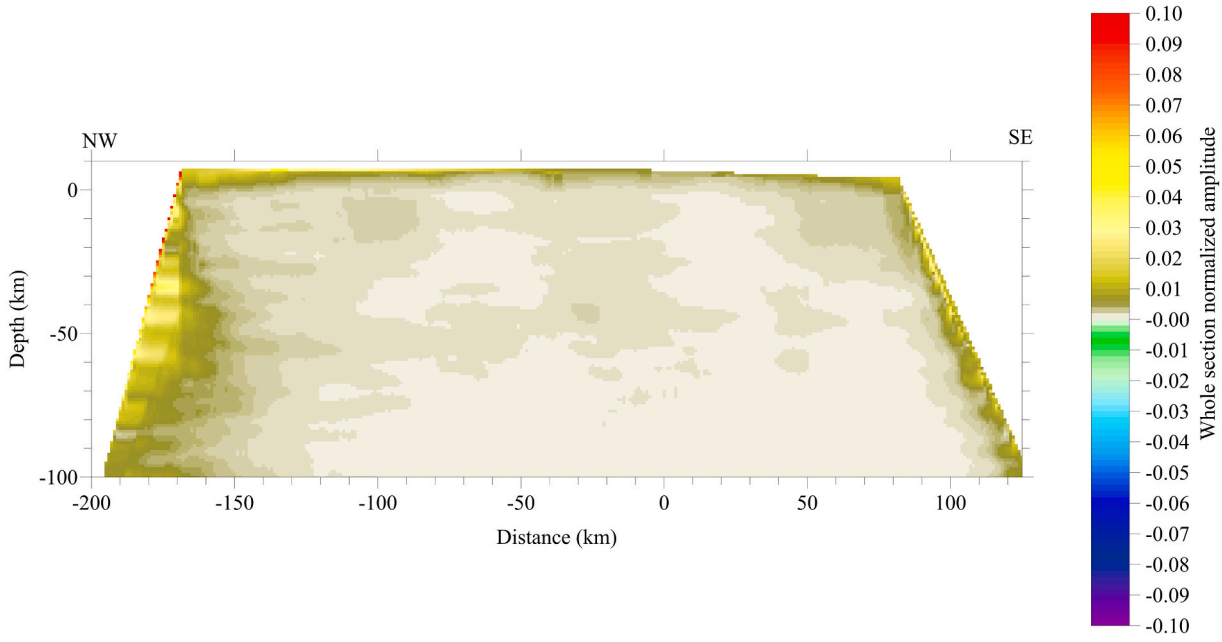

Fig. 5. Standard deviation of 50 depth migrations obtained using the bootstrap method with replacement for the receiver function data from the 2018–2020 profile.

wide (effectively infinite) perpendicular to and on either side of the profile and 3 km in depth. This compares with 24, 50 and 6 km for the transect *E*-F for the 2012–2013 data (Fig. 4b). Once all the rays were traced and the respective boxes filled, the amplitudes were normalized by dividing by the number of traces contributing to the total amplitude in each box. This means that the individual receiver functions are reweighted to a certain extent. Receiver functions from the same back azimuth and distance are downweighted as they contribute to the amplitudes in the same boxes with many trace hits and receiver functions from poorly covered back azimuth and distance ranges are upweighted when they contribute to the amplitudes in boxes with only a small number of trace hits. Varying the size of the boxes does not change the result significantly. Lastly, the data were interpolated to produce the final image shown (Fig. 4a).

The bootstrap method was applied in order to provide a measure for the robustness of the depth migration method described above and also to calculate standard deviations for the migration images. This involved randomly sampling the receiver functions with replacement to obtain a bootstrap sample following Sacchi (1998). A migration image was then derived from this bootstrap sample as described above. This procedure was repeated 50 times and then the average and standard deviation at each point of the images were calculated. The standard deviations are shown along the profile for the 2018–2020 data (Fig. 5). The image shows that the standard deviations are almost always below 0.005. The exceptions are at the edges of the profile. All the features that are interpreted below to be significant have absolute amplitudes that are greater than 0.01 and thus are generally larger than twice the standard deviation.

Fig. 4 shows receiver function migration images from the two deployments. From the 2018–2020 data, the Moho occurs at about 45 km depth beneath the Sichuan basin and at about 55 km depth below the Songpan-Ganzi terrane of the Tibetan plateau (Fig. 4a). This is in broad agreement with the Moho depths from profile *E*-F of the 2012–2013 data (Fig. 4b). Also, the negative converter in the lower crust beneath both the Sichuan basin and the Songpan-Ganzi terrane is present in both images, although it appears to be fainter above the Moho step in the 2018–2020 data. There is no new significant information regarding these negative converters in this study with respect to that of Qian et al. (2018), in which these features were quite extensively discussed. Within the Sichuan basin the conversion from the base of the Mesozoic sediments in the top 10 km can be recognized in both images, although it is more prominent in the 2012–2013 data than in the 2018–2020 data. In contrast, profile E-F of the first 3-D array deployment (Qian et al., 2018) showed a dislocation and overlap of the Moho at a distance of about −50 km, whereas the profile of the second deployment shows a dislocation but no overlap at the same distance. The new profile shows a negative converter in the upper crust at about 15 km depth beneath the Pengguan Complex, which was not apparent in the section from the first deployment. This negative conversion can be recognized in the summed trace of the observed data for station LMS32 at about 1.75 s delay time (Fig. 3). The projection of aftershocks of the Wenchuan earthquake is distributed around this conversion. Thus, it would seem possible that this conversion marks the boundary between the high velocity material of the Pengguan Complex and low velocity material below and that this boundary is flat-lying and, in fact, a faulted boundary or detachment. The detachment may continue to the SW of the Pengguan Complex as indicated by the aftershocks but then through a region with no velocity contrast. The faults observed at the surface presumably then branch off the detachment as steep-angle faults, since further horizontal movement is obstructed by the Sichuan basin. At around the WMF, the negative converter below the Pengguan Complex appears to deepen by about 3 km and merge with another negative converter at about 18 km depth. This negative converter continues at around 17–23 km depth to the NW end of the profile with a gap of about 20 km, 50–70 km NW of the WMF, and was also recognized on the profiles of the 2012–2013 data (Qian et al., 2018), including profile E-F (Fig. 4b). Again, the negative conversion can be seen in the summed traces of the observed data for stations LMS43 and LMS55 at around 1.75 s delay time (Fig. 3).

4. Tomography of both deployments

A tomographic image of P-wave velocities was obtained by fitting the travel times of local earthquake and teleseismic data. The forward problem employed the Fast Marching ray-tracing algorithm (Rawlinson et al., 2006; Rawlinson and Urvoy, 2006) with a Moho interface, to obtain the theoretical travel times and Frechet derivatives. The inversion was carried out by sequential quadratic programming (Boggs and Tolle, 1995), using the MATLAB routine fmincom. Here, the objective function to be minimized was the difference between the observed travel times and the travel times produced by a given (initial) model with

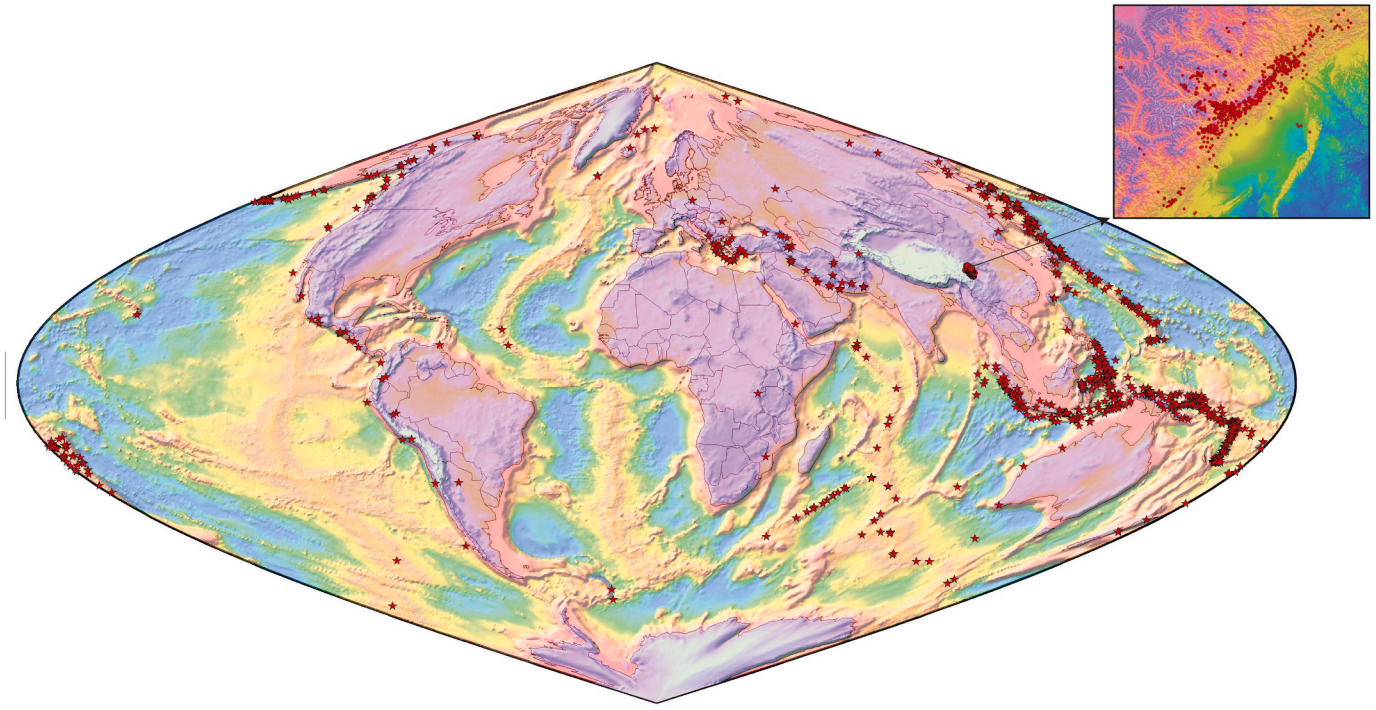

Fig. 6. Maps of teleseismic events and local events used for the 3-D tomographic inversion.

Table 1
Initial velocity-depth model used in the three dimensional inversion (modified after Qian et al. (2016), Table 2).

Depth (km)	Velocity (km/s)	Layer
−15.000	4.0000	Crust
0.000	5.2000	Crust
10.000	5.9000	Crust
20.000	6.300	Crust
34.000	6.700	Crust
34.000	6.9200	Crust
47.600	7.200	Crust
47.600	8.1100	Mantle
77.500	8.1400	Mantle
120.000	8.1700	Mantle

boundary conditions that limit the extent to which velocities and Moho depths can change.

In total 953 local events and 1308 teleseismic events were utilized for the inversion (Fig. 6). A minimum of four P-wave picks was required from each local or teleseismic event which then resulted in a total of 34,115 local P-wave picks and 47,675 teleseismic P-wave picks. The accuracy for the local P-wave picks was estimated to be 0.07 s while for the teleseismic P-wave picks it was estimated to be 0.1 s. The model ranged from 101°E to 106.5°E in longitude, 29°N to 33.5°N in latitude and − 7 km to 87.8 km in depth. The topographic difference between the Sichuan basin and the Tibetan plateau was taken into account. The model comprised 110 equally spaced nodes each in longitude and latitude, and 32 equally spaced nodes in depth for the forward problem using the Fast Marching ray-tracing method. For the inversion, the model comprised 55 equally spaced nodes each in longitude and latitude and 16 equally spaced nodes in depth.

The initial velocity model was one dimensional in each of the two model layers, namely crust and mantle (Table 1). The Moho interface between the two layers in the initial model was three dimensional and was derived by interpolation of the results from H-K stacking (Qian et al., 2015). During the inversion the root mean square (rms) travel-time residual reduced from 0.46 s for the initial model to 0.22 s for the final three dimensional model.

Horizontal velocity slices (Fig. 7) show that high velocities occupy the Longmenshan, a mixture of high and low velocities occupy the Songpan-Ganzi terrane and low velocities occupy the Sichuan basin in the upper crust as illustrated by the slice at 0 km depth. This pattern is generally the same at 20 km depth, although the high velocities of the Longmenshan are much less prominent. In the lower crust the horizontal velocity slice at 40 km depth shows that the Songpan-Ganzi terrane has a large range of low velocities whereas the Sichuan basin has predominantly high velocities, especially in its western portion, and represents the rigid Lower Yangtze plate. Four cross-sections (Fig. 8) all show that the Pengguan Complex is rooted at about 15 km depth and is a high velocity block limited by the WMF and YBF. Local earthquakes are mainly distributed around the Pengguan Complex and along the interface between high and low velocities at about 15 km depth. Below about 20 km depth, in the middle and lower crust, the Songpan-Ganzi terrane is generally characterized by low velocities and the Sichuan basin is generally characterized by high velocities, especially in its western portion. The boundary between the high and low velocities generally occurs NW of the surface trace of the YBF.

In order to estimate the resolving power of the seismic network, a checkerboard test was carried out (Fig. 9). Checkers of 20 km size in longitude, 20 km in latitude and 20 km in depth with alternating velocity perturbations of ±0.4 km/s were constructed. Then, theoretical travel times were calculated using the Fast Marching ray-tracing method. Then random noise with standard deviations of ±0.1 s for the teleseismic events and ± 0.07 s for the local earthquakes was added to the travel times. Finally, an inversion similar to that used for the real data was carried out. The results of the checkerboard test show that the checker anomalies can be best retrieved in the upper crust (see horizontal slice at 0 km depth in Fig. 9) and that resolution decreases with depth. Perhaps the most important point to be gleaned from this test is that despite the smearing along the trend of the Longmenshan, the high velocity block about 100 km long, 30 km wide and 20 km deep covering the extent of the Pengguan complex (Figs. 7–8) should be resolvable. Thus, a model recovery test was attempted. For this, a high velocity block 100 km long, 30 km wide, 20 km deep and with an increase in P-

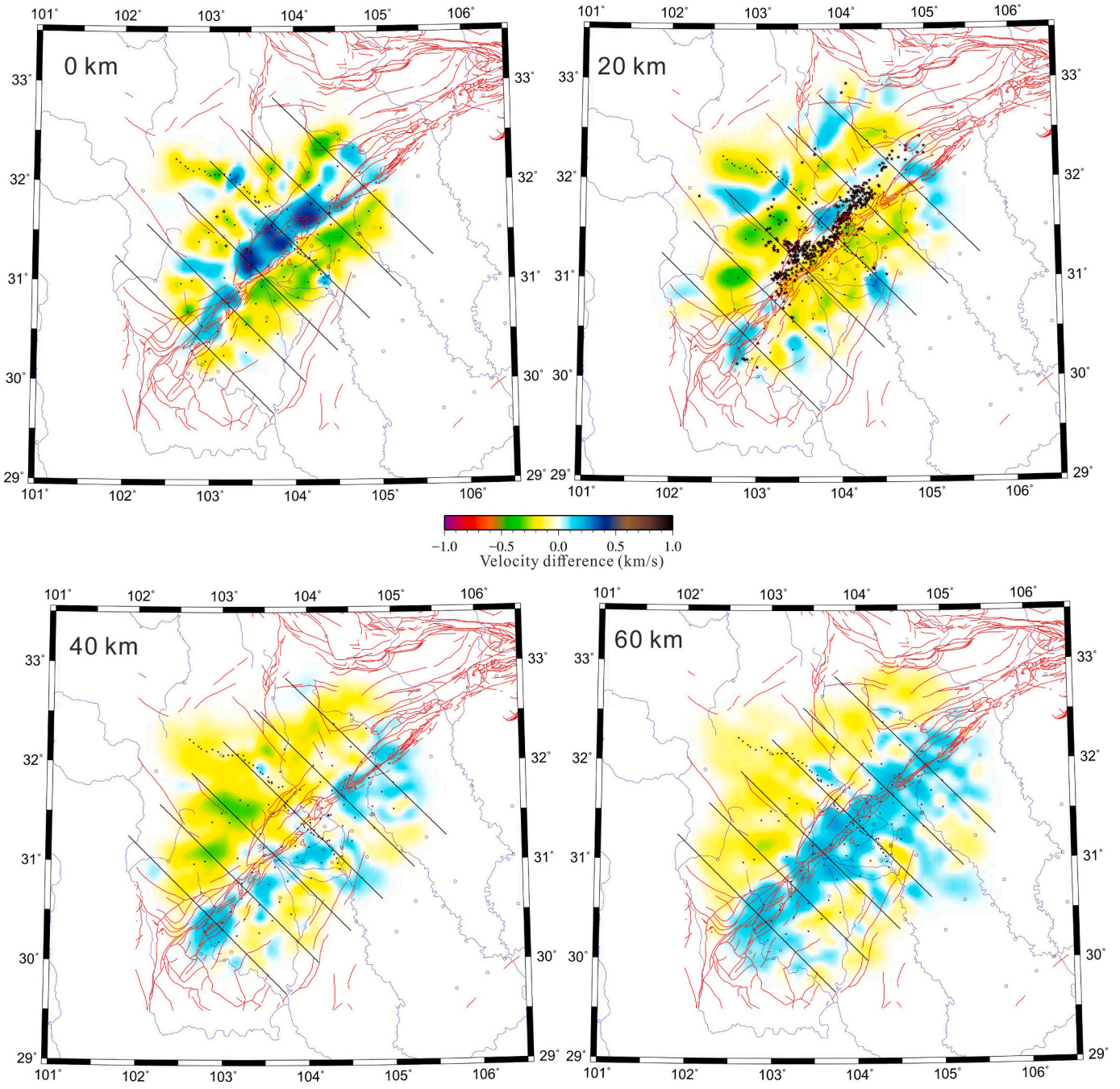

Fig. 7. Horizontal slices through the tomographic image at 0, 20, 40 and 60 km depths. (For interpretation of the references to color in this figure legend, the reader is referred to the web version of this article.)
Red lines represent faults. Inverted triangles represent the seismic stations. Stars represent the local earthquakes used in the inversion.

wave velocity of 0.5 km/s with respect to the surrounding material served as input. The results of this test, which was carried out similar to the checkerboard test, show that the high velocity anomaly can be recovered quite well (Fig. 10). There is some smearing laterally but very little vertically. Synthetic receiver functions through the high velocity block show a negative pulse from the base of the block at about 2–2.5 s delay time (Fig. 10). As in the observed data for station LMS32 (Fig. 3), the amplitude of this negative pulse is quite significant compared to the positive pulse of the Moho which occurs at 5–5.5 s delay time. For the calculation of the receiver functions the crustal S-wave velocities were set to be equal to the P-wave velocities divided by 1.732 and the uppermost mantle S-wave velocity was set to 4.4 km/s. The fact that the synthetic negative pulse at 2–2.5 s delay time is a little later than that at about 1.75 s delay time in the observed data for station LMS32 can be explained by the synthetic anomaly probably being about 5 km deeper than the actual anomaly (Figs. 4 and 8).

5. Discussion

5.1. Style of Moho depth increase

All the controlled source seismic profiles crossing the Longmenshan fault zone show a fairly smooth increase in crustal thickness from the Sichuan basin in the SE to the Tibetan plateau in the NW (e.g. Wang et al., 2007, 2013, 2015a; Guo et al., 2013; Xu et al., 2016). At about 31.6°N, a near-vertical incidence reflection profile (Guo et al., 2013), a

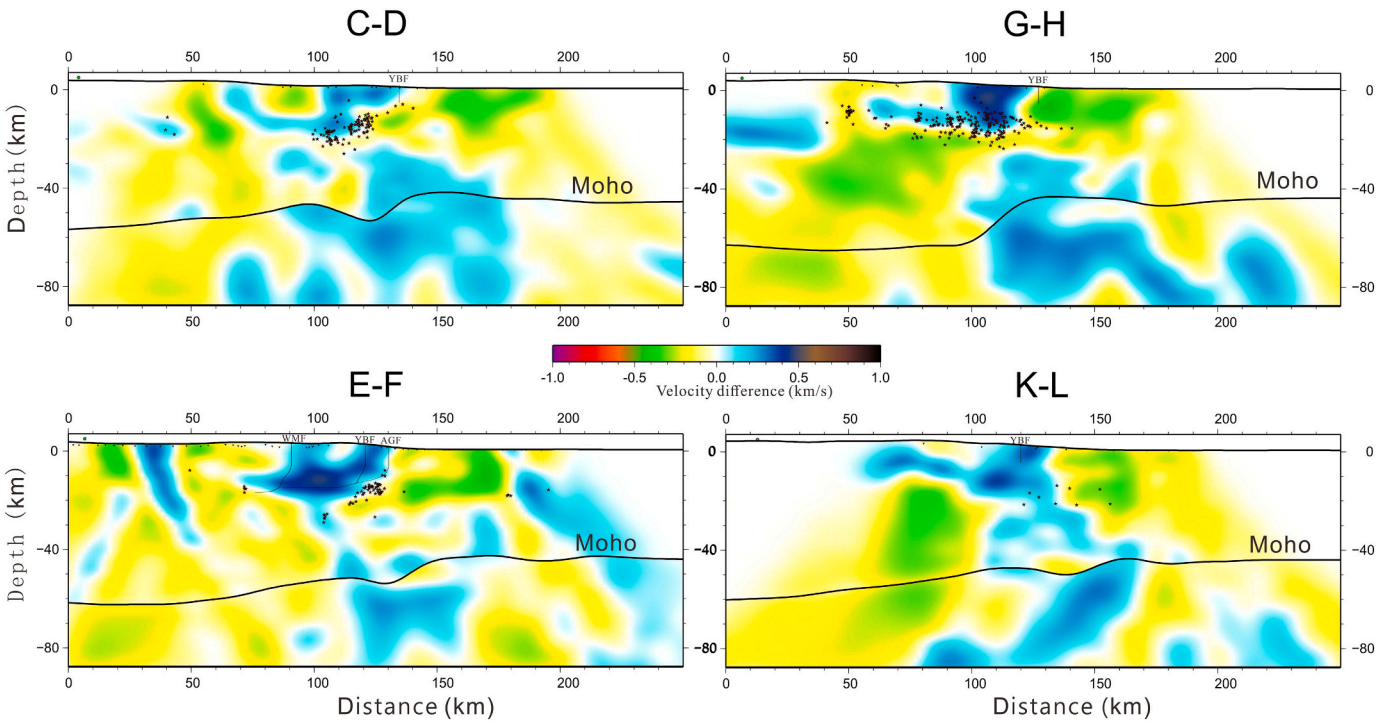

Fig. 8. Cross-sections through the tomographic image.
Black dots represent local earthquakes, within ±10 km of the cross-sections, used in the inversion. Thin black lines in cross-section E-F represent faults whose abbreviations are as in Fig. 1. The location of the surface exposure of the YBF is shown in the other cross-sections. For the locations of the cross-sections, see Fig. 1.

refraction/wide-angle reflection profile (Xu et al., 2016) and a receiver function profile (profile C-D of Qian et al., 2018) cross the YBF. Here a relatively smooth increase in Moho depth can be observed from the SE to the NW from the results using all three methods, with a maximum offset of the Moho of about 5 km. Southwest of 31.5°N along the YBF, the refraction/wide-angle reflection profiles also show a smooth increase in Moho depth from SE to NW (Jia et al., 2014; Wang et al., 2007, 2013, 2015a). In contrast, the profiles based mainly on receiver function studies (e.g. Zhang et al., 2009, 2010; Robert et al., 2010; Liu et al., 2014; Qian et al., 2018) show more abrupt changes across the Longmenshan fault zone and in some cases a Moho step has been identified (Zhang et al., 2009, 2010; Liu et al., 2014; Qian et al., 2018). In this study using the receiver function method, the Moho step is identified about 50 km NW of the YBF (Fig. 4a), and it is possible that even some overlap of the Moho can be found associated with this step, as shown by the cross-section (Fig. 4b) from Qian et al. (2018). With respect to the difference in the Moho structure between Fig. 4a & b, it should perhaps be stated that of the three profiles of Qian et al. (2018) which showed overlap of the Moho, this one (Fig. 4b) showed the least amount of overlap.

The difference between the results from the controlled and passive source studies may be, at least partly, due to the differences in the methods. The receiver function method uses low frequency (<1 Hz), steeply incoming rays whereas the refraction/wide-angle reflection method uses higher frequency (>1 Hz) rays which travel a significant part of their path more or less horizontally and thus average structure laterally. Further, in some cases the shot-point density in the refraction/wide-angle reflection experiments may have been insufficient to discriminate between a smooth deepening of the Moho and an abrupt deepening or step. This could be the case in the experiment of Wang et al. (2013) where the shots were spaced more than 100 km apart and thus may not have been optimally placed to image an abrupt deepening of the Moho across the Longmenshan fault zone. On the other hand, in the case of Jia et al. (2014) and Wang et al. (2015a) this should not have been the case. Jia et al. (2014) had nine shots with an average spacing of 20 km and Wang et al. (2015a) had six shots with an average spacing of 20–25 km across the Longmenshan fault zone. What is missing in this region is a near-vertical incidence reflection profile with resolution all the way through the crust to the Moho.

5.2. *Pengguan complex*

From the tomographic image of this study, the Pengguan Complex is characterized by high P-wave velocities in the upper crust down to about 15 km depth between the YBF and WMF (Figs. 7–8). Below about 15 km depth the high velocity anomaly dies out and, in fact, P-wave velocity decreases at the base of the anomaly (Fig. 8). From the receiver function analysis in this study, a negative converter, indicating a decrease in S-wave velocity with depth, is detected at about 15 km depth beneath the Pengguan Complex (Fig. 4a). Previous studies have also found high velocities associated with the Pengguan Complex. Using local earthquake tomography, Wang et al. (2015b) found high P- and S-wave velocities down to about 20 km depth associated with the Pengguan Complex between the YBF and WMF. Using ambient noise tomography, Feng et al. (2021) also found high S-wave velocities in the upper crust associated with the Pengguan Complex. The reason why the negative converter at about 15 km depth beneath the Pengguan Complex has been detected in this study and not in that of Qian et al. (2018) may be the higher station density in this study, despite the gap of about 20 km across the central Pengguan Complex between stations LMS16 and LMS27 (Fig. 1).

The tomography and receiver function images point to a change from high velocity to low velocity with depth and that the boundary is more or less horizontal at about 15 km depth. This could mark the base of the high velocity Pengguan Complex lying above material with lower velocities. As the aftershocks of the Wenchuan earthquake correlate well with the negative converter and the base of the high velocity anomaly in the tomographic image, it is plausible that the boundary between the high velocity Pengguan Complex and the low velocity material beneath is not just a lithological boundary but also a faulted boundary or

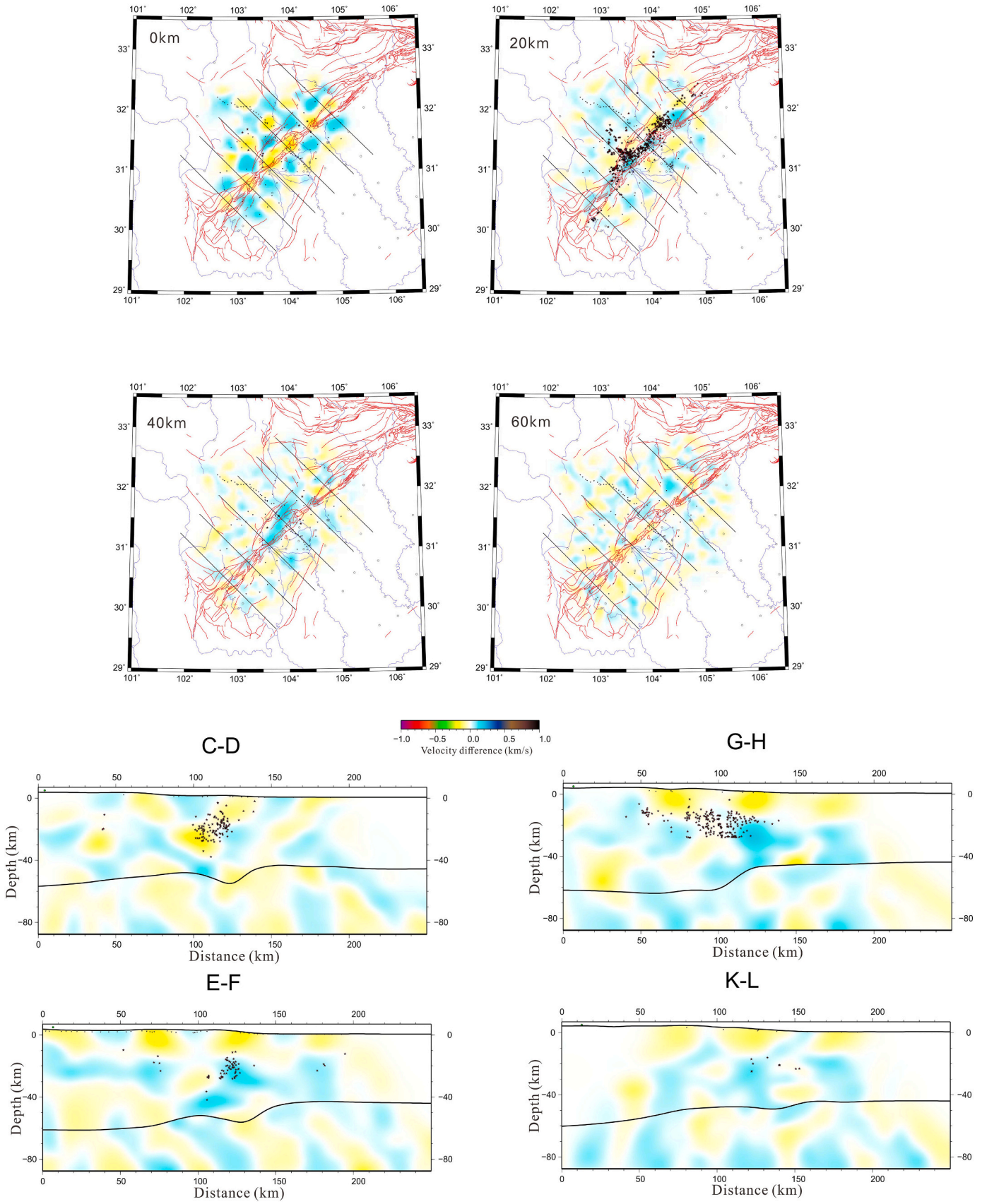

Fig. 9. Horizontal and vertical slices through the checkerboard test.
Horizontal slices are at 0, 20, 40 and 60 km depth. For locations of vertical slices, see Fig. 1. In the horizontal slices, red lines represent faults, inverted triangles represent the seismic stations and stars represent local earthquakes. In the vertical cross-sections, black dots represent local earthquakes, within ±10 km of the cross-sections, used in the inversion.

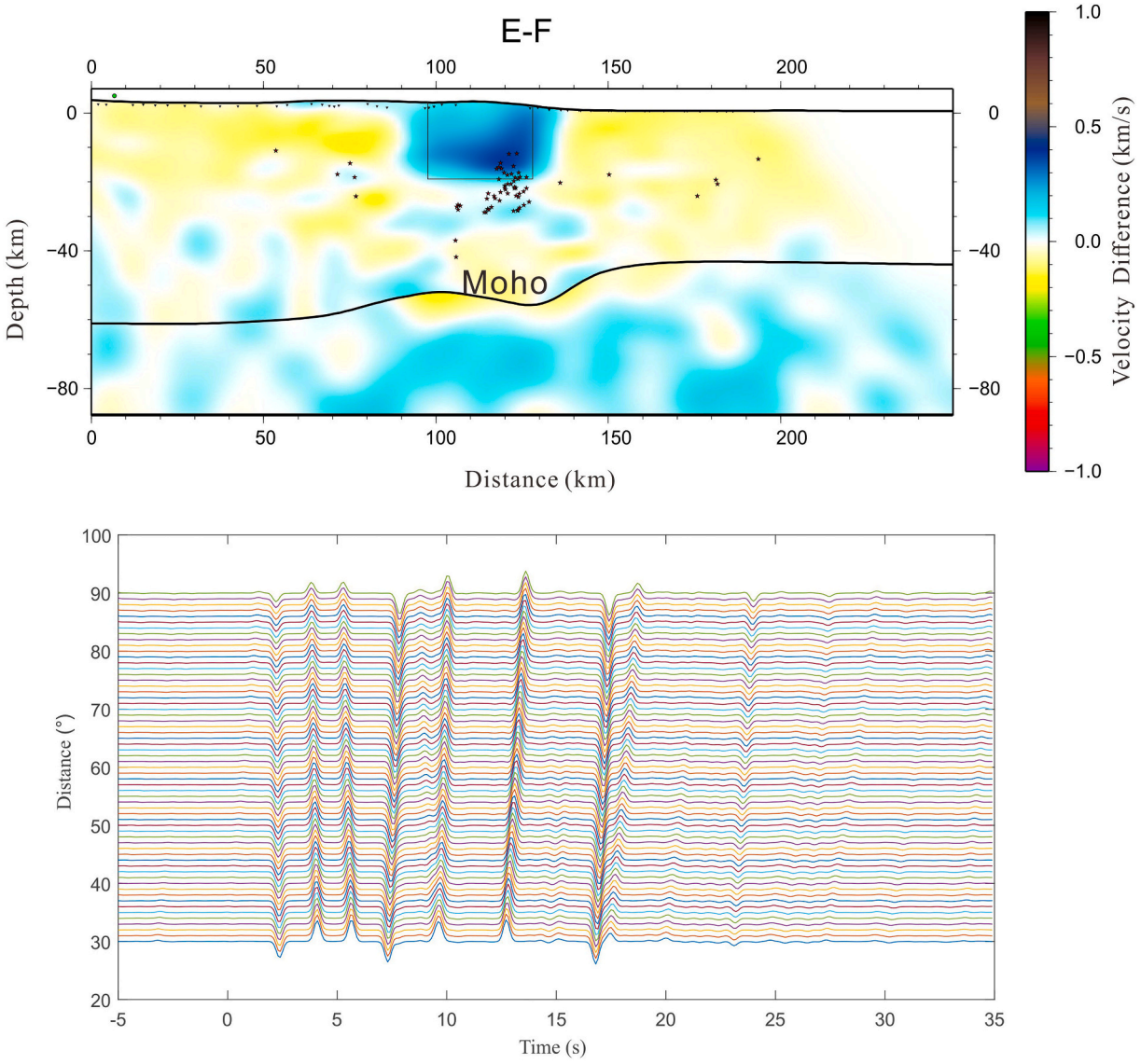

Fig. 10. Cross-section through the model recovery test for the high velocity anomaly of the Pengguan Complex along profile E-F (top) and synthetic receiver functions for the high velocity anomaly of the Pengguan Complex (bottom).
The black line shows the outline of the input high velocity anomaly with a P-wave velocity increase of 0.5 km/s with respect to the surrounding material. Black dots represent local earthquakes, within ±10 km of the cross-section, used in the inversion. For location of the cross-section, see Fig. 1.

detachment zone. The depth of such a detachment is the same as that postulated by Jia et al. (2010) and Li et al. (2010). Jia et al. (2010) and Li et al. (2010) also postulated that the detachment continues to the SW under the Sichuan basin to explain the occurrence of aftershocks SW of the YBF and that the faults observed at the surface e.g. the YBF or AGF, branch off the detachment as steep-angle faults.

In agreement with Wang et al. (2015b), the tomographic image in this study shows that the high P-wave velocities typical of the Pengguan Complex disappear NW of the WMF. The negative converter at about 15 km depth below the Pengguan Complex seems to deepen at around the WMF by about 3 km and merge to the NW with another negative converter at about 18 km depth. This negative converter to the NW of the WMF was also recognized in the 2012–2013 data (Qian et al., 2018) and was interpreted to represent the top of the ubiquitous Tibetan mid-crustal low velocity zone (Yang et al., 2012). Results from magneto-telluric studies across the Longmenshan fault zone in the region (Li and Jin, 1987; Zhao et al., 2012) show a layer with high conductivity beneath the eastern Tibetan plateau, that terminates about 25 km NW of the WMF. The depth of the top of the high conductivity layer is about 20 km and is thus similar to that of the negative converter NW of the WMF at around 18 km. Spatially, the two features overlap to within about 25 km NW of the WMF. The mid-crustal, low velocity, high conductivity layer has been interpreted as being due to the presence of a combination of partial melts, aqueous fluids and aligned anisotropic minerals and thus should be mechanically weak (Yang et al., 2012; Zhao et al., 2012). As stated by Zhao et al. (2012) it could very well localize and accommodate deformation occurring along a detachment beneath the Pengguan Complex and the steep-angle faults that branch off such a detachment.

5.3. *Connection between the upper and deeper crust*

At about 31.6°N, Guo et al. (2013) and Xu et al. (2016) showed the Longmenshan fault cutting through the crust at a high angle to connect the point where the WMF and YBF join at depth to a step in the Moho about 30 km to the NW. Guo et al. (2013) stated that below the upper crust the fault may continue as a ductile shear zone down towards the Moho. In this respect, it is perhaps interesting to note that earthquakes

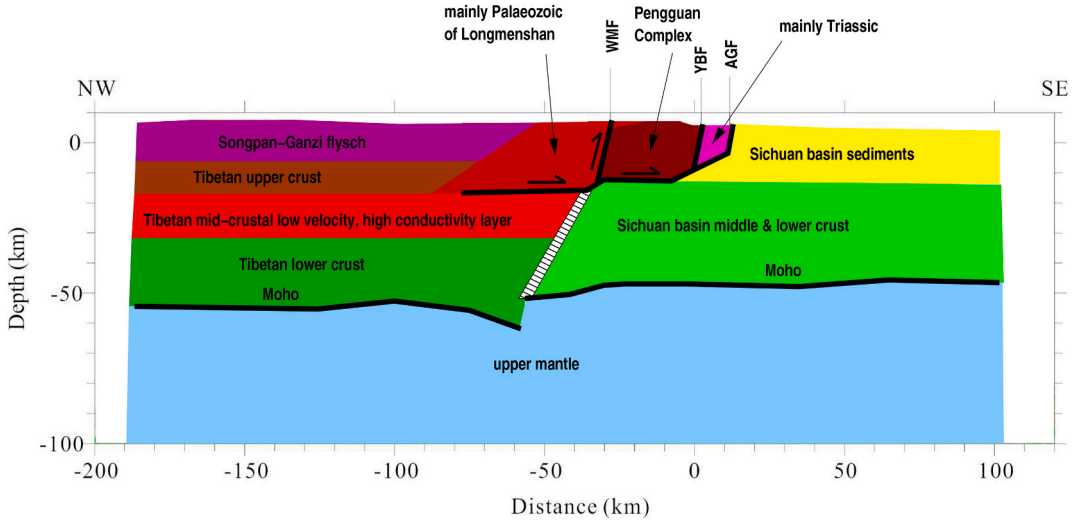

Fig. 11. Simple geological cross-section through the Longmenshan along the 2018–2020 profile.
Black lines show the Moho and faults whose abbreviations are as in Fig. 1.

are much more seldom in the middle and lower crust below about 20 km depth than in the upper crust (Figs. 4a and 8). The tomography results (Fig. 8) show that the boundary between the low velocities of the Songpan-Ganzi terrane and the high velocities of the Sichuan basin in the middle and lower crust occurs NW of the surface trace of the YBF. Further, the P-wave velocity maps of Wang et al. (2015b) derived by local earthquake tomography show that the boundary between the low velocities of the Songpan-Ganzi terrane and the high velocities of the Sichuan basin in the middle and lower crust occurs approximately below the surface trace of the WMF. Taking the converter NW of the WMF to represent the top of the Tibetan mid-crustal low velocity zone and bearing in mind the tomographic results and the results of magneto-telluric surveys (e.g. Zhao et al., 2012), a zone of distributed, possibly ductile, deformation extending through the middle and lower crust is shown along the 2018–2020 profile (Fig. 11). This zone extends from the WMF at about 15 km depth to the Moho step and marks the boundary in the middle and lower crust between the Sichuan basin to the SE and the Tibetan plateau to the NW. The Longmenshan fault zone is not only a zone in which thrust movement occurs but also a zone in which strike-slip movement occurs (e.g. Burchfiel et al., 1995; Li et al., 2018). In this respect, it is perhaps interesting that a study at the Dead Sea Transform (Rümpker et al., 2003), where strike-slip movement is dominant, showed that a vertical boundary layer about 20 km wide accommodates the movement in the mantle beneath the predominantly brittle crust, between the Arabian plate to the east and the African plate to the west.

6. Conclusions

Through the joint data processing from two deployment periods of seismic stations in the Longmenshan area, receiver function and tomographic images have been obtained. From these images and a comparison with existing results, the following conclusions have been drawn (Fig. 11).

1) The Moho shows a significant change in depths across the boundary between the Sichuan basin and the Tibetan plateau, and at the location of the 2018–2020 profile forms an abrupt step and possibly even shows overlap to some extent.
2) The Pengguan Complex appears as a high velocity block in the upper crust between the YBF and WMF.
3) At the base of the Pengguan Complex, a flat-lying boundary at about 15 km depth has been detected, at which velocity decreases downwards. Aftershock locations of the Wenchuan earthquake correlate well with the boundary. Thus, the boundary may well represent a detachment zone, from which the steep-angle faults e.g. AGF, YBF and WMF, observed at the surface branch off.
4) Below about 20 km depth in the middle and lower crust, the Songpan-Ganzi terrane of the Tibetan plateau is generally characterized by low velocities and the Sichuan basin is generally characterized by high velocities especially in its western portion.
5) It is proposed that a zone of distributed deformation occurs between the SE end of the top of the Tibetan mid-crustal low velocity, high conductivity zone just to the NW of the WMF and the Moho step about 25 km further NW. This deformation zone may at least be partly ductile as indicated by the paucity of earthquakes below about 20 km depth.

Author statement

Hui Qian: data processing, modelling and interpretation, manuscript organization and writing

James Mechie: project design and management (Germany), data modelling and interpretation, manuscript writing

Changqing Yu: project design and management (China), instrument management, manuscript editing

Xiangzhi Zeng: field work, data collection, manuscript editing.

Declaration of Competing Interest

The authors declare that they have no known competing financial interests or personal relationships that could have appeared to influence the work reported in this paper.

Acknowledgements

This work was supported by grant 41761134096 from the National Natural Science Foundation of China and by grant ME 1570/6-1 from the Deutsche Forschungsgemeinschaft (DFG) – project number 391957130. The Geophysical Instrument Pool of the Deutsches GeoForschungsZentrum Potsdam – GFZ is acknowledged for providing the instruments for the 2018-2020 field experiment. The data from the 50 German instruments from the 2012-2013 field experiment (FDSN code 2F 2012-2013) are archived at the GEOFON Data Centre (Qian and Mechie, 2012). These data are publicly available. The data from the 30 Chinese stations from the 2012-2013 field experiment are archived in

China. Permission to use these data should be sought through H.Q. from the Chinese Geological Survey. The data from the 2018-2020 field experiment (FDSN code 4O 2018-2020) are archived at the GEOFON data centre (Yu and Mechie, 2021). These data will become publicly available in January 2024.

References

Boggs, P.T., Tolle, J.W., 1995. Sequential quadratic programming. Acta Numer. 4, 1–51.

Burchfiel, B.C., Chen, Z.L., Liu, Y.P., et al., 1995. Tectonics of the Longmen Shan and adjacent regions, Central China. Int. Geol. Rev. 37 (8), 661–735. https://doi.org/10.1080/00206819509465424.

Cook, K.L., Royden, L.H., Burchfiel, B.C., Lee, Y.-H., Tan, X., 2013. Constraints on Cenozoic tectonics in the southwestern Longmen Shan from low-temperature thermochronology. Lithosphere 5 (4), 393–406.

Dueker, K.G., Sheehan, A.F., 1997. Mantle discontinuity structure from midpoint stacks of converted P to S waves across the Yellowstone hotspot track. J. Geophys. Res. 102, 8313–8327.

Dueker, K.G., Sheehan, A.F., 1998. Mantle discontinuity structure beneath the Colorado Rocky Mountains and High Plains. J. Geophys. Res. 103, 7153–7169.

Feng, Y.Y., Yu, C.Q., Fan, Z.G., et al., 2016. Fine crustal structure of the Lushan area derived from seismic reflection profiling. Chin. J. Geophys. (in Chinese) 59 (9), 3248–3259. https://doi.org/10.6038/cjg20160910.

Feng, M., Qian, H., Mechie, J., An, M., Li, H., Xue, G., Su, H., Cui, X., 2021. Crustal seismogenic structures and deformation styles along the Longmen Shan Fault belt in the eastern Tibetan Plateau inferred from ambient noise tomography. Tectonophysics 798, 228689. https://doi.org/10.1016/j.tecto.2020.228689.

Guo, X., Gao, R., Keller, G.R., Xu, X., Wang, H., Li, W., 2013. Imaging the crustal structure beneath the eastern Tibetan Plateau and implications for the uplift of the Longmen Shan range. Earth Planet. Sci. Lett. 379 (5), 72–80.

Jia, D., Li, Y.Q., Lin, A.M., Wang, M., Chen, W., Wu, X., Ren, Z., Zhao, Y. & Luo, L. Structural model of 2008 M_W 7.9 Wenchuan earthquake in the rejuvenated Longmen Shan thrust belt, China, Tectonophysics, 2010, 491(1–4): 174–184.

Jia, S.X., Liu B.J., Xu, Z.F., Liu, Z., Feng, S.Y, Zhang, J.S., Lin, J.Y., Tian, X.F., Liu, Q.X. & Guo, W.B. The crustal structures of the central Longmenshan along and its margins as related to the seismotectonics of the 2008 Wenchuan Earthquake, Sci. China Earth Sci., 2014, 57: 777–790, doi:https://doi.org/10.1007/s11430-013-4744-9.

Herrmann, R.B., 2013. Computer programs in seismology: An evolving tool for instruction and research. Seism. Res. Lettr. 84, 1081–1088. http://www.eas.slu.edu/eqc/eqccps.html.

Kennett, B.L.N., Engdahl, E.R., 1991. Traveltimes for global earthquake location and phase identification. Geophys. J. Int. 105, 429–465.

Kind, R., Kosarev, G.L., Petersen, N.V., 1995. Receiver functions at the stations of the German Regional Seismic Network (GRSN). Geophys. J. Int. 121, 191–202.

Kumar, P., Yuan, X., Kind, R., Ni, J., 2006. Imaging the colliding Indian and Asian lithospheric plates beneath Tibet. J. Geophys. Res. 111, B06308. https://doi.org/10.1029/2005JB003930.

Li, L., Jin, G.Y., 1987. Telluric electromagnetic sounding study of crust and upper mantle in the Panxi Rift Zone and the Longmenshan Faulted Zone. Geophys. Geochem. Explor. 11 (3), 161–169.

Li, Y., Jia, D., Shaw, J.H., Hubbard, J., Lin, A., Wang, M., Luo, L., Li., H. & Wu, L., 2010. Structural interpretation of the coseismic faults of the Wenchuan earthquake: Three-dimensional modeling of the Longmen Shan fold-and-thrust belt. J. Geophys. Res. 115, B04317. https://doi.org/10.1029/2009JB006824.

Li, H., Wang, H., Xu, Z., Si, J., Pei, J., Li, T., Huang, Y., Song, S.-R., Kuo, L.-W., Sun, Z., Chevalier, M.-L., Liu, D., 2013. Characteristics of the fault-related rocks, fault zones and the principal slip zone in the Wenchuan Earthquake Fault Scientific Drilling Project Hole-1 (WFSD-1). Tectonophysics 584 (1), 23–42.

Li, H., Xu, Z., Niu, Y., Kong, G., Huang, Y., Wang, H., Si, J., Sun, Z., Pei, J., Gong, Z., Chevalier, M.-L., Liu, D., 2014a. Structural and physical property characterization in the Wenchuan earthquake Fault Scientific Drilling project — hole 1 (WFSD-1). Tectonophysics 619–620, 86–100.

Li, Y., Jia, D., Wang, M., Shaw, J.H., He, J., Lin, A., Xiong, L., Rao, G., 2014b. Structural geometry of the source region for the 2013 Mw 6.6 Lushan earthquake: Implication for earthquake hazard assessment along the Longmen Shan, Earth Planet. Sci. Lett. 390 (4), 275–286.

Li, H., Wang, H., Yang, G., Xu, Z., Li, T., Si, J., Sun, Z., Huang, Y., Chevalier, M.-L., Zhang, W., Zhang, J., 2016. Lithological and structural characterization of the Longmen Shan fault belt from the 3rd hole of the Wenchuan Earthquake Fault Scientific Drilling project (WFSD-3). Int. J. Earth Sci. 105 (8), 2253–2272.

Li, Z., Zhang, P., Zheng, W., Jia, D., Hubbard, J., Almeida, R., Sun, C., Shi, X., Li, T., 2018. Oblique thrusting and strain partitioning in the Longmen Shan fold-and-thrust belt, eastern Tibetan plateau. J. Geophys. Res. 123, 4431–4453. https://doi.org/10.1029/2018JB015529.

Liu, C.P., Lin, J.H., 2008. Study on the forming model of Pengguan complex of the Longmenshan orogenic belt. Inn. Mongol. Petrochem. Industry 34 (19), 41–43.

Liu, Q.Y., van der Hilst, R.D., Li, Y., Yao, H.J., Chen, J.H., Guo, B., Qi, S.H., Wang, J., Huang, H., Li, S.C., 2014. Eastward expansion of the Tibetan Plateau by crustal flow and strain partitioning across faults. Nat. Geosci. 7, 361–365. https://doi.org/10.1038/ngeo2130.

Lu, R., He, D., John, S., Wu, J.E., Liu, B., Chen, Y., 2014. Structural model of the central Longmen Shan thrusts using seismic reflection profiles: Implications for the sediments and deformations since the Mesozoic. Tectonophysics 630, 43–53.

Ma, Y.W., Wang, G.Z., Hu, X.W., 1996. Tectonic deformation of Pengguan complex as a nappe. Acta Geol. Sichuan. 16 (2), 110–114.

Qian, H., Mechie, J., 2012. Temporary seismological network in Longmenshan, China (2012/2013). In: Deutsches GeoForschungsZentrum GFZ Other/Seismic Network. https://doi.org/10.14470/7S7567431325.

Qian, H., Li, H., Mechie, J., Xue, G., Su, H., Cui, X., 2015. H-k stacking of receiver functions and its application in a portable array along the Longmen mountains. Progr. Geophys. (in Chinese) 30 (1), 91–98. https://doi.org/10.6038/pg20150114.

Qian, H., Mechie, J., Li, H., Xue, G., Su, H., Cui, X., 2016. An approach to jointly invert hypocenters and 1-D velocity structure and its application to the Lushan earthquake series. J. Seismol. 20, 213–232.

Qian, H., Mechie, J., Li, H., Xue, G., Su, H., Cui, X., 2018. Structure of the Crust and Mantle down to 700 km Depth beneath the Longmenshan from *P* Receiver Functions. Tectonics 37 (6), 1688–1708.

Rawlinson, N., Urvoy, M., 2006. Simultaneous inversion of active and passive source datasets for 3-D seismic structure with application to Tasmania. Geophys. Res. Lett. 33, L24313. https://doi.org/10.1029/2006GL028105.

Rawlinson, N., de Kool, M., Sambridge, M., 2006. Seismic wavefront tracking in 3-D heterogeneous media: applications with multiple data classes. Explor. Geophys. 37, 322–330.

Robert, A., Zhu, J., Vergne, J., Cattin, R., Chan, L.S., Wittlinger, G., Herquel, G., de Sigoyer, J., Pubellier, M., Zhu, L.D., 2010. Crustal structures in the area of the 2008 Sichuan earthquake from seismologic and gravimetric data. Tectonophysics 491, 205–210.

Rümpker, G., Ryberg, T., Bock, G., 2003. Boundary-layer mantle flow under the Dead Sea transform fault inferred from seismic anisotropy. Nature 425, 497–501.

Sacchi, M.D., 1998. A bootstrap procedure for high-resolution velocity analysis. Geophysics 63, 1716–1725.

Wang, C.Y., Han, W.B., Wu, J.P., Lou, H., Chan, W.W., 2007. Crustal structure beneath the eastern margin of the Tibetan Plateau and its tectonic implications. J. Geophys. Res. 112 (B7), B07307. https://doi.org/10.1029/2005JB003873.

Wang, Y., Mooney, W.D., Yuan, X., Okaya, N., 2013. Crustal structure of the northeastern Tibetan Plateau from the Southern Tarim Basin to the Sichuan Basin, China. Tectonophysics 584, 191–208.

Wang, S.-J., Wang, F.-Y., Zhang, J.-S., Liu, B.-F., Zhang, C.-K., Zhao, J.-R., Duan, Y.-L., Song, X.-H., Deng, X.-G., Ma, C.-J., Sun, Y.-N., Zang, Y.-R., Li, Y.-Q., 2015a. A study of deep seismogenic environment in Lushan Ms7.0 earthquake zone by wide-angle seismic reflection/refraction profile. Chin. J. Geophys. 58, 474–485.

Wang, Z., Su, J., Liu, C., Cai, X., 2015b. New insights into the generation of the 2013 Lushan Earthquake (M_s 7.0), China. J. Geophys. Res. 120, 3507–3526. https://doi.org/10.1002/2014JB011692.

Wang, M., Hubbard, J., Plesch, A., Shaw, J.H., Wang, L., 2016. Three-dimensional seismic velocity structure in the Sichuan basin, China. J. Geophys. Res. 121, 1007–1022. https://doi.org/10.1002/2015JB012644.

Weislogel, A., 2008. Tectonostratigraphic and geochronologic constraints on evolution of the northeast Paleotethys from the Songpan-Ganzi complex, Central China. Tectonophysics 451, 331–345.

Wu, C., Li, H., Leloup, P.H., Yu, C., Si, J., Liu, D., Pan, J., Chevalier, M.-L., Gong, Z., 2014. High-angle fault responsible for the surface ruptures along the northern segment of the Wenchuan Earthquake Fault Zone: evidence from the latest seismic reflection profiles. Tectonophysics 619–620, 159–170.

Xu, X., Keller, G.R., Gao, R., Guo, X., Zhu, X., 2016. Uplift of the Longmen Shan area in the eastern Tibetan plateau: an integrated geophysical and geodynamic analysis. Int. Geol. Rev. 58 (1), 14–31.

Yang, Y., Ritzwoller, M.H., Zheng, Y., Shen, W., Levshin, A.L. & Xie, Z. A synoptic view of the distribution and connectivity of the mid-crustal low velocity zone beneath Tibet. J. Geophys. Res., 117, B04303, doi:https://doi.org/10.1029/2011JB008810.

Yu, C., Mechie, J., 2021. Seismological profile across Longmenshan fault – LONGMEN-P (2018-2020). GFZ Data Serv. Other/Seismic Netw. https://doi.org/10.14470/9B7563261622.

Yu, M.Y., Yu, C.Q., Qu, C., Wang, Q., Zeng, X.Z., Tian, Z.Y., Zheng, X.J., 2021. Deep structural characteristics of Pengguan complex in Longmenshan fault zone derived from seismic reflective profile. Earth Sci. China 46 (5), 1737–1748. http://kns.cnki.net/kcms/detail/42.1874.P.20200305.1734.014.html.

Yuan, X., 2000. Teleseismic receiver function study and its application in Tibet and the Central Andes. PhD thesis. In: FU Berlin, Scientific Technical Report / GeoForschungsZentrum Potsdam STR00/10.

Yuan, X., Ni, J., Kind, R., Mechie, J., Sandvol, E., 1997. Lithospheric and upper mantle structure of southern Tibet from a seismological passive source experiment. J. Geophys. Res. 102, 27491–27500.

Zhang, P.-Z., Shen, Z., Wang, M., Gan, W., Bürgmann, R., Molnar, P., Wang, Q., Niu, Z., Sun, J., Wu, J., Hanrong, S., Xinzhao, Y., 2004. Continuous deformation of the Tibetan Plateau from global positioning system data. Geology 32, 809–812.

Zhang, Z., Wang, Y., Chen, Y., Houseman, G.A., Tian, X., Wang, E., Teng, J., 2009. Crustal structure across Longmenshan fault belt from passive source seismic profiling. Geophys. Res. Lett. 36 (17), 1397–1413.

Zhang, Z., Yuan, X., Chen, Y., Tian, X., Kind, R., Li, X., Teng, J., 2010. Seismic signature of the collision between the east Tibetan escape flow and the Sichuan Basin. Earth Planet. Sci. Lett. 292 (4), 254–264.

Zhao, G., Unsworth, M.J., Zhan, Y., Wang, L., Chen, X., Jones, A.G., Tang, J., Xiao, Q., Wang, J., Cai, J., Li, T., Wang, Y., Zhang, J., 2012. Crustal structure and rheology of the Longmenshan and Wenchuan Mw 7.9 earthquake epicentral area from magnetotelluric data. Geology 40, 1139–1142. https://doi.org/10.1130/G33703.1.